JOURNAL OF SPACECRAFT AND ROCKETS
Vol. 51, No. 3, May–June 2014

Analysis of Navier–Stokes Codes Applied to Supersonic Retropropulsion Wind-Tunnel Test

Kerry A. Zarchi*
NASA Ames Research Center, Moffett Field, California 94035
Daniel G. Schauerhamer†
Jacobs Technology, Inc., Houston, Texas 77058
and
William L. Kleb,‡ Jan-Renee Carlson,§ and Karl T. Edquist¶
NASA Langley Research Center, Hampton, Virginia 23681

DOI: 10.2514/1.A32744

Advancement of supersonic retropropulsion as a technology will rely heavily on the ability of computational methods to accurately predict vehicle aerodynamics during atmospheric descent, where supersonic retropropulsion will be employed. A wind-tunnel test at the NASA Langley Unitary Plan Wind Tunnel was specifically designed to aid in the support of Navier–Stokes codes for supersonic retropropulsion applications. Three computational fluid dynamics codes [data parallel line relaxation, fully unstructured Navier–Stokes three-dimensional, and overset grid flow solver] were exercised for multiple nozzle configurations for a range of freestream Mach numbers and nozzle thrust coefficients. The computational fluid dynamics pretest analysis of this wind-tunnel test aided in the test model design process by identifying the potential for tunnel blockage or unstart, of liquefaction within the plume, and of separation occurring at the internal fingers of the nozzles. This analysis led to a reduced model diameter, heating of the plenum, and reducing the nozzle area ratio, and the requirement to radius the corners at the fingers, to counter these potentials, respectively. Comparisons to test data were used to determine the existing capability of the codes to accurately model this complex flow, identify modeling shortcomings, and gain insight into the computational requirements necessary for correctly computing these flows. All three codes predict similar surface pressure coefficients and flowfield structures, such as jet termination shock, interface, bow shocks, and recirculation regions. However, the codes differ on the level of unsteadiness predicted.

Nomenclature

A_{ref}	=	reference area, πr_b^2, in.^{2}
C_p	=	pressure coefficient
C_T	=	thrust coefficient, $T/(q_\infty A_{\text{ref}})$
M_∞	=	freestream Mach number
q_∞	=	freestream dynamic pressure, psia
r	=	radial coordinate, in.
r_b	=	model radius, in.
T	=	thrust, lbf
x	=	axial coordinate, in.
α	=	angle of attack, deg
ϕ	=	model cylindrical angle, deg

I. Introduction

SUPERSONIC retropropulsion (SRP) is a potentially viable alternative means for deceleration of high-mass vehicles entering the Martian atmosphere [1–6]. Deceleration technologies, such as parachutes, are not scalable for exploration class vehicles that are large (>20 m diameter) and can potentially weigh tens of metric tons. Because ground or flight testing SRP technology at conditions relevant to Mars entry can be difficult and expensive, the advancement of this technology will depend heavily on the ability of computational fluid dynamics (CFD) to predict the flowfield and resulting aerodynamics and aerothermodynamics. The present study was performed to aid in the design of an SRP wind-tunnel model and test, to perform an initial rough assessment of CFD capabilities to accurately predict SRP flowfields, and to identify shortcomings of CFD predictions. This is the first step in what will become a series of validation efforts. Please refer to [7–9] for a continuation of this work, which focuses on validation and testing efforts of these CFD codes.

Supersonic flowfields containing a combination of oncoming and counterflowing streams, such as in SRP, have a complex structure involving shocks, shear layers, recirculation, and stagnation regions. The concept is schematically illustrated in Fig. 1 for a single nozzle configuration. In this illustration, a supersonic freestream is being opposed by a jet emanating from a body, which forces the bow shock off from the body, a recirculation region develops at the region of shear layer and jet termination shock interaction. Jarvinen and Adams [10] described the characteristics of a single SRP jet flowfield. The principal parameter used to characterize the interaction of the jet plume with the opposing freestream is the thrust coefficient ($C_T = T/q_\infty A_{\text{ref}}$), where T is thrust, q_∞ is freestream dynamic pressure, and A_{ref} is reference area ($A_{\text{ref}} = \pi r_b^2$). The complex interaction between the jet plume and external flowfield is expected to stress numerical accuracy of the existing CFD codes and will drive further development in numerous areas, including grid generation/adaption and turbulence modeling. The complexities of the flow, with shocks, shear layers, and recirculation and stagnation regions, make it a challenge for flow prediction tools. The validation process chosen by the SRP team includes using multiple CFD codes to compare to historic and recent wind-tunnel tests [11–13]. Code-to-code and code-to-test comparisons, based on good practices in gridding, numerical method selection, and solution advancement, help reduce

Received 22 June 2013; revision received 20 February 2014; accepted for publication 21 February 2014; published online 10 April 2014.

*Aerospace Engineer, Aerothermodynamics Branch, Mail Stop 230-2. Senior Member AIAA.
†Aerospace Engineer, Applied Aeroscience and Computational Fluid Dynamics Branch, EG3; currently NASA Johnson Space Center. Member AIAA.
‡Aerospace Engineer, Aerothermodynamics Branch, Mail Stop 408A. Lifetime Member AIAA.
§Aerospace Engineer, Computational Aerosciences Branch, Mail Stop 128. Senior Member AIAA.
¶Aerospace Engineer, Atmospheric Flight and Entry Systems Branch, Mail Stop 489. Senior Member AIAA.

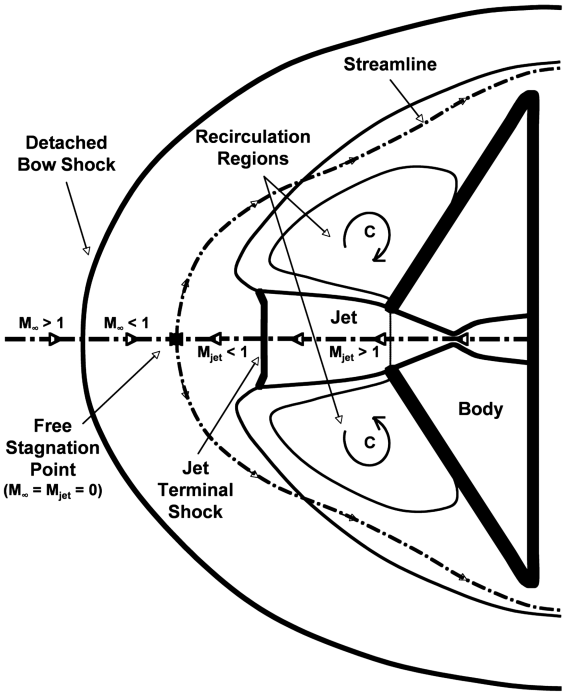

Fig. 1 SRP jet plume characteristics described by Korzun and Braun for a single jet configuration [5].

uncertainties in the computations, thereby allowing the focus to be on the physics of the flowfields and validity of the math models. With validation of predictive tools against ground-based tests, confidence can be built in their ability to model SRP flow and they can be applied with more certainty to an actual flight entry in the continuum flow regime.

Preliminary CFD assessment and development has been leveraged from an existing SRP fluid dynamics knowledge base, which consists primarily of an unrelated series of wind-tunnel tests on blunt bodies during the Apollo and Viking eras [11]. These historic wind-tunnel tests are incomplete, have many inconsistencies, and typically are not detailed enough for comprehensive CFD analysis. For instance, static conditions are recorded but dynamics of the interactions between the freestream and the plume are not mentioned at all. In light of these shortcomings, it was determined that new wind-tunnel experiments are required to provide higher fidelity data for CFD validation exercises that demonstrate modeling strengths and weaknesses. The wind-tunnel experiment described here is designed specifically to qualitatively and quantitatively determine the capability of the CFD codes, data parallel line relaxation (DPLR) [14], fully unstructured Navier–Stokes three-dimensional (FUN3D) [15,16], and overset grid flow solver (OVERFLOW) [17], in characterizing supersonic

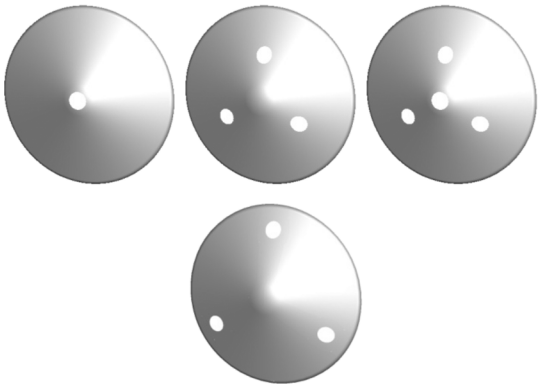

Fig. 2 Initial nozzle configurations: (left) single, (middle top) three at one-half radial location, (middle bottom) at three-quarters radial location, and (right) four.

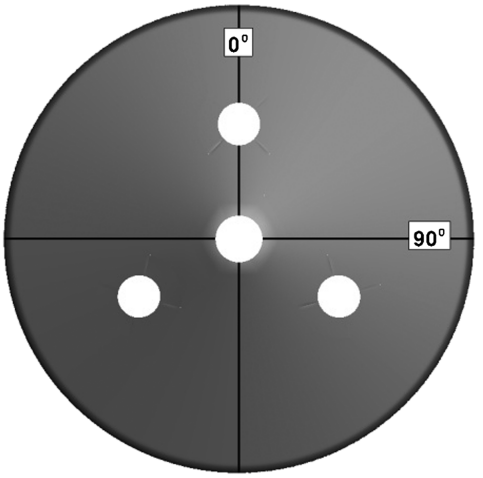

Fig. 3 Location of data slices (at $\phi = 0$ and 90 deg) relative to the nozzles. Shown on the four-nozzle configuration model.

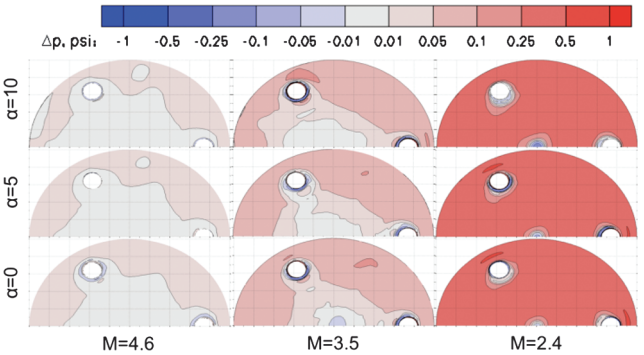

Fig. 4 Subset of FUN3D solutions for pretest wind-tunnel model design for thrust coefficient of 10. Contours are surface pressure differences between solutions with and without tunnel walls.

retropropulsion physical phenomenon. The first in a series of tests, the NASA Langley Unitary Plan Wind Tunnel (UPWT) test was successful. The test series consisted of three different Mach numbers, several angles of attack and thrust coefficients for four nozzle configurations [18]. The NASA Langley Research Center UPWT test, however, was limited in the maximum thrust coefficient that could be reached due to size constraints of the test section. The 4×4 ft^2 test section contributed to wall interference effects, and even tunnel blockage, for thrust coefficients greater than three for some configurations, which was anticipated by the pretest CFD shown within.

The three CFD codes are being tested for both single- and multiple-nozzle configurations for a range of Mach numbers and thrust coefficients. The present paper will discuss the model design process for the NASA Langley UPWT experiment, including the influence of pretest CFD on model diameter and radial location of periphery nozzles. The paper will also discuss the pretest CFD analysis to determine the effects, if any, of the tunnel wall interference and possible liquefaction within the plumes. For further discussion on the design of the experiment, please refer to the article by Berry et al. [18].

II. Computational Methods

CFD is a valuable means of determining important design factors such as aerodynamics and aerothermodynamics. These analyses are leveraged to design vehicle systems such as guidance, navigation, and control and thermal protection systems on full-scale vehicles. It is important that the CFD tool's accuracy and limitations are well understood. The SRP team has employed three different CFD codes (DPLR, FUN3D, and OVERFLOW) to assess their respective capabilities for simulating SRP flows. The codes differ in implementation, grid type, and numerical methods. All codes assume the fluid flow to be perfect

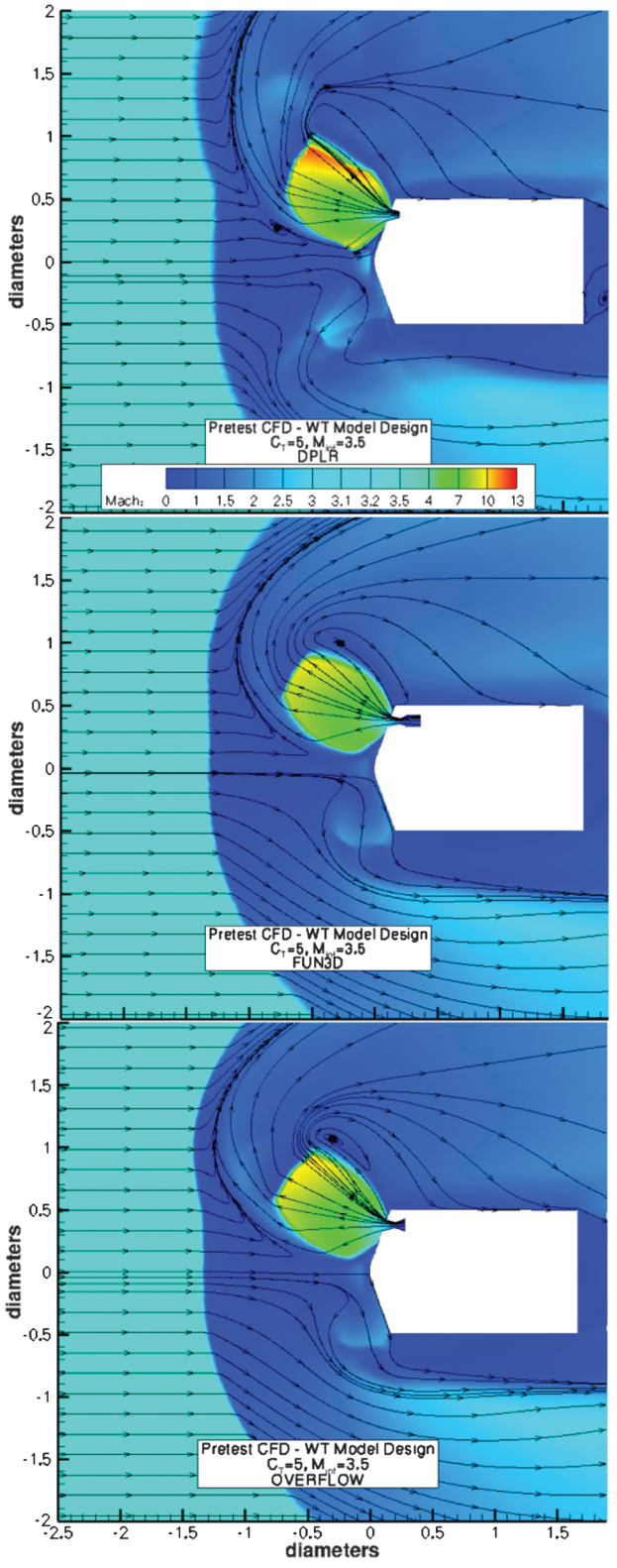

Fig. 5 Mach contours for 6-in.-diam, three-quarters radial periphery configuration wind-tunnel (WT) model design at $M_\infty = 3.5$ and $C_T = 5$.

gas in the presented results. DPLR and OVERFLOW modeled a full three-dimensional geometry, whereas FUN3D modeled half-geometry with a symmetry plane. A detailed analysis of grid and solution convergence determined for each CFD code was investigated more completely in [8]. A brief summary of each code is given below.

A. DPLR

The DPLR CFD code [14] is a parallel, multiblock structured mesh, finite volume code that solves the Navier–Stokes equations for

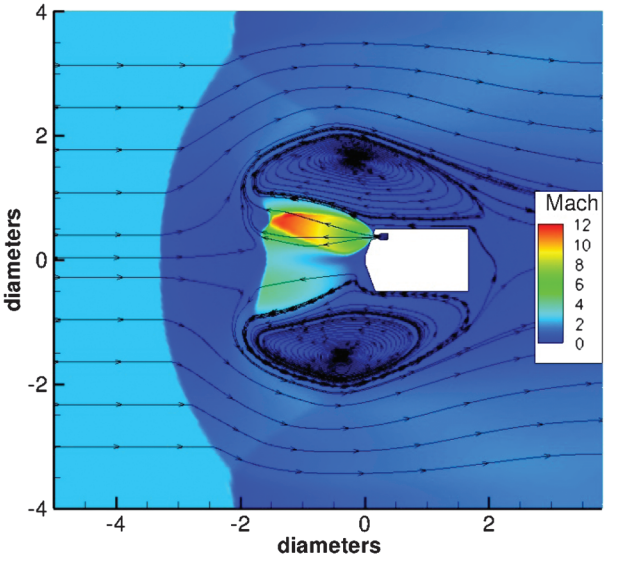

Fig. 6 Potential tunnel blockage due to 6-in.-diam model at $M_\infty = 2.4$ and $C_T = 10$ as predicted with FUN3D. Bounds on the y axis are locations of tunnel walls, modeled inviscidly.

continuum flow, including the effects of finite rate chemistry and thermal nonequilibrium. In the present study, the equations are solved implicitly in time with first-order accuracy. Euler fluxes are computed using modified Steger–Warming flux vector splitting [19] with third-order spatial accuracy via MUSCL extrapolation with a minmod limiter [20]. The viscous fluxes are computed with second-order spatial accuracy using a central difference approach. For the present analysis, the shear-stress transport (SST) turbulence model [21] was employed with a vorticity-based production term. The presented results are computed with point-matched grid systems. Solution convergence for the steady pretest cases was determined when negligible differences (±1 psi in surface pressure) in the solution between iterations was observed. A grid study was performed by refining the grid until there were no longer differences in solutions between grid resolution levels [8].

B. FUN3D

The FUN3D suite of codes contains a node-based finite volume flow solver [15,16]. The FUN3D website** contains the user manual and an extensive list of references. FUN3D can solve unsteady, incompressible and compressible, Euler and Navier–Stokes flow with thermo-chemical nonequilibrium. The present study employs Edwards's low-diffusion flux-splitting scheme [22] with a Van Albada limiter [21] to solve the compressible Reynolds-averaged Navier–Stokes (RANS) equations coupled to Menter's SST turbulence model. The SST model employed here is strain based. All node-based conservative variables are computed by driving a second-order-accurate spatial residual to steady state with a point-implicit iterative method. For steady flows, local time stepping is employed, and for unsteady flows, up to fourth-order time accuracy is available via subiterations. FUN3D can use general mixed-element grids and overset grid systems, but only tetrahedral grids are used in this study. Solution convergence was determined when negligible differences in the solution were observed between iterations. Grid convergence was determined in the form of observed spatial order of accuracy by monitoring two error quantities as a function of grid resolution [8].

C. OVERFLOW

OVERFLOW 2 [17] is an implicit RANS flow solver that uses structured overset grids [23,24]. Several Euler flux schemes are available, including central differencing and a number of upwind schemes [25,26]. Implicit time advance schemes include block

**Data available online at http://fun3d.larc.nasa.gov [retrieved 4 June 2013].

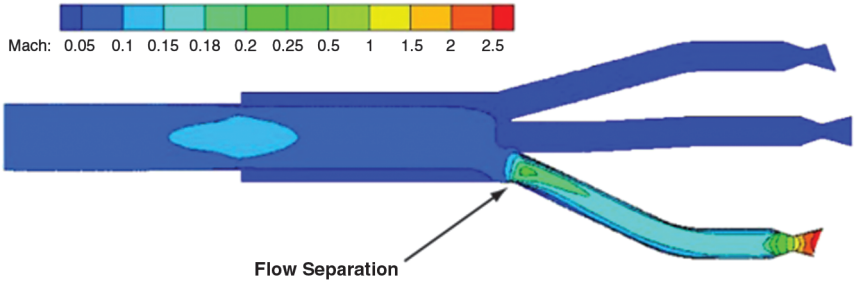

Fig. 7 Mach contours on symmetry plane from FUN3D internal solution for early plenum and nozzle design with seven fingers.

Fig. 8 Final model design mounted in tunnel. Zero-nozzle configuration is shown.

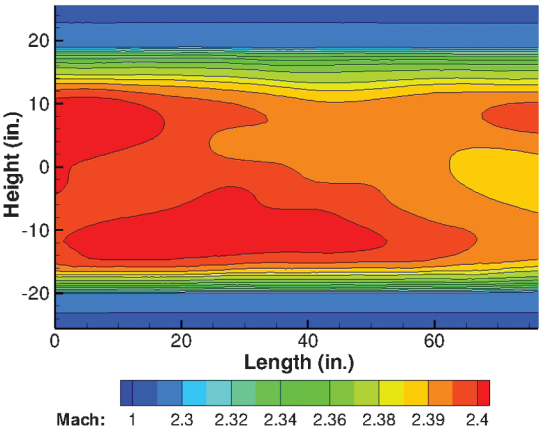

Fig. 9 Wind-tunnel test section Mach contours illustrating the thickness of boundary layer at the walls, as predicted by FUN3D.

tridiagonal alternating direction implicit (ADI), scalar pentadiagonal ADI [27], and symmetric successive overrelaxation method (SSOR) [28]. Newton subiteration or dual time stepping can be used for second-order time-accurate simulations [28,29]. Turbulence models include Baldwin–Barth [30], Spalart–Allmaras [31], and SST. Other OVERFLOW capabilities include automatic domain decomposition and partitioning for parallel processing [32,33], automatic off-body grid generation with adaptation [34,35], grid sequencing, and multigrid low-Mach preconditioning, a full six-degree-of-freedom solver with collision detection [36,37], and the ability to solve applications with multiple species. For the current work, the numerical flux function HLLE++ (Harten, Lax, van Leer, and Einfeldt) [38] with the Van Albada limiter [39] was used for spatial terms, and the SSOR algorithm with dual time stepping using Newton subiterations was used for temporal terms. The strain-based SST turbulence model was employed. The overall scheme is second-order accurate in space and time. The inviscid flux calculations for both the flow solver and the turbulence model use third-order-accurate MUSCL extrapolation. Solution convergence was determined when negligible differences in the solution between iterations occurred. Grid convergence was determined by employing a global refinement factor, and was considered to be reached when a solution had negligible differences between grid levels [8].

Table 1 Pretest CFD case matrix, prioritizing number of nozzles, angle of attack (AOA), freestream Mach number, and thrust coefficient

Priority	Nozzles	AOA (deg)	Mach	C_T
1	0	0, 2, 10	2.4	0
2			3.5	0
3			4.6	0
4	1	0	2.4	5
5				10
6	1	0	4.6	5
7				10
8	1	10	2.4	5
9				10
10	1	10	4.6	5
11				10
12	3	0	2.4	5
13				10
14	3	0	4.6	5
15				10
16	4	0	2.4	5
17				10
18	4	0	4.6	5
19				10
20	4	10	2.4	5
21				10
22	4	10	4.6	5
23				10
24	1	2	2.4	5
25				10
26	1	2	4.6	5
27				10
28	4	2	2.4	5
29				10
30	4	2	4.6	5
31				10

III. Wind-Tunnel Model Design

The Langley Unitary Plan Wind Tunnel (4×4 ft test section) was chosen for its relatively large test section and flight relevant Mach number range (2.4–4.6 in test section 2). The model was initially chosen to be a 70 deg sphere cone with a 6 in. diameter and a cylindrical afterbody. A 6 in. model would have ample internal volume for the air distribution system and instrumentation. The nozzle configuration would allow for zero nozzle, single nozzle at center of the model, two three-nozzle configurations at different radial locations on the periphery of the model, and two four-nozzle configurations, which include the center nozzle and either of the three peripheral nozzle configurations (Fig. 2). The three peripheral nozzles would be located at the one-half and three-quarters radial locations. The rays through the center of the model to the shoulder will be characterized with ϕ, where 0 deg intersects at the top of the model and 90 deg is at the right (Fig. 3). The experiment design was aided by CFD to refine the model scale, determine effects of tunnel

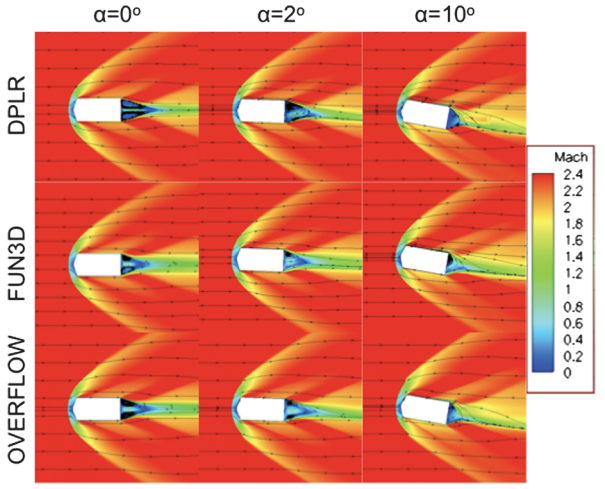

Fig. 10 Zero-nozzle configuration Mach contours at 0, 2, and 10 deg angles of attack at $M_\infty = 2.4$.

walls, and assess the nozzle configurations. The CFD model assessment case matrix included freestream Mach numbers of 2.4, 3.5, and 4.6, thrust coefficients of 0, 5, and 10, and angles of attack of 0, 5, and 10 deg. During the initial evaluation, the single nozzle and both three-nozzle configurations were analyzed.

The effects of the tunnel walls on the surface pressure of the model are greatly dependent on the model diameter and thrust coefficient. In the case of a large model diameter (6 in.) with large thrust coefficient ($C_T > 10$), the tunnel could become blocked, causing it to unstart or contaminate the freestream. Initial results for the 6-in.-diam model with the three-nozzle configuration at the three-quarters radial location suggest that the walls would greatly influence the surface quantities and possibly even unstart the tunnel (large region of subsonic flow). To investigate wall effects, a 4-in.-diam model was analyzed.

Figure 4 shows FUN3D solutions that demonstrate the effect of tunnel walls, modeled inviscidly, on surface pressure distributions. The plots show differences in surface pressure between simulations with and without tunnel walls for a thrust coefficient of 10, freestream Mach numbers of 2.4, 3.5, and 4.6, and angle of attack at 0, 5, and 10 deg. In the figure, the white sections represent no difference between the simulations, indicating no influence from the tunnel walls. The large red and some blue pockets are noted, which show at least a 1 psi of pressure difference between simulations with and without walls. For these cases, modeling of the tunnel walls would be necessary in the CFD simulations. A viscous tunnel wall simulation was performed to look at the boundary layer (shown and discussed in more detail later).

DPLR and OVERFLOW were used on a subset of these cases, including an overlapping case for all codes of the 6-in.-diam, three-nozzle, three-quarters radial periphery configuration wind-tunnel model at $M_\infty = 3.5$ and $C_T = 5$ (Fig. 5). FUN3D and OVERFLOW are in agreement on the

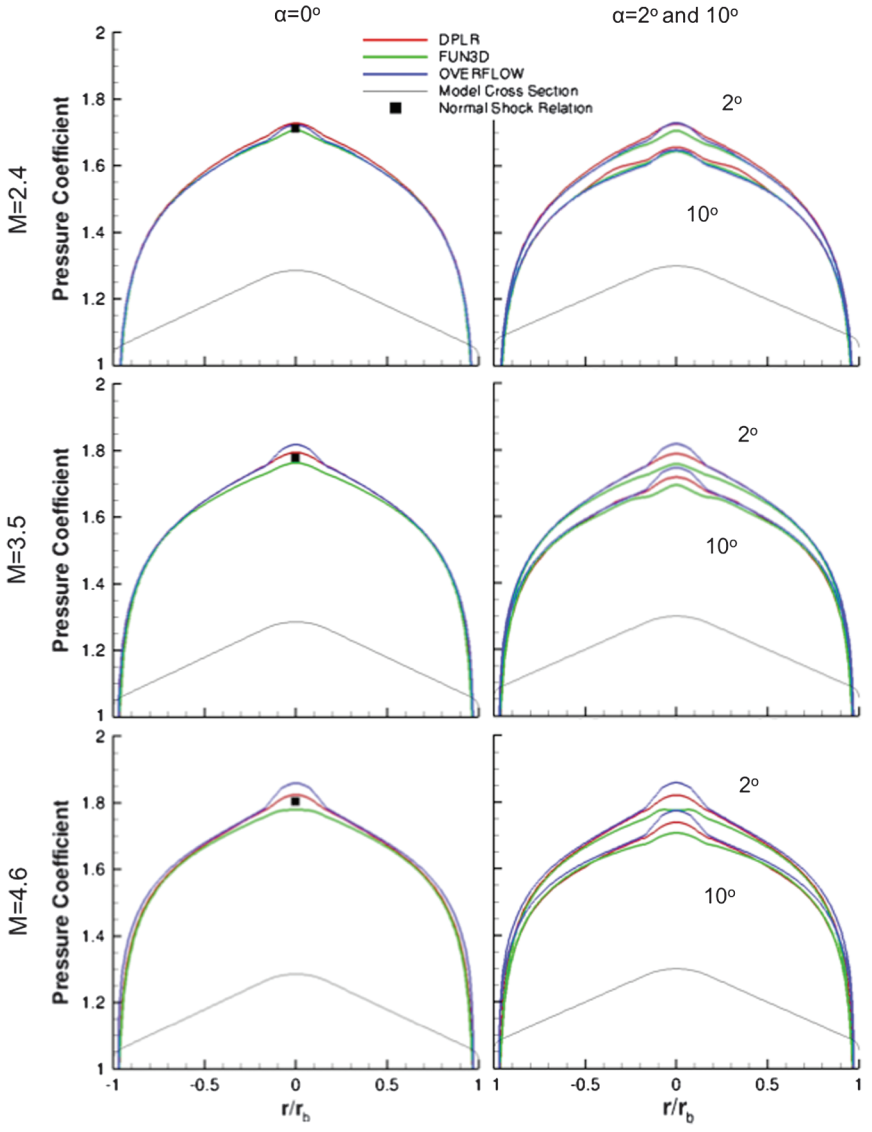

Fig. 11 Pressure coefficient slices at $\phi = 90$ deg for zero-nozzle configuration model.

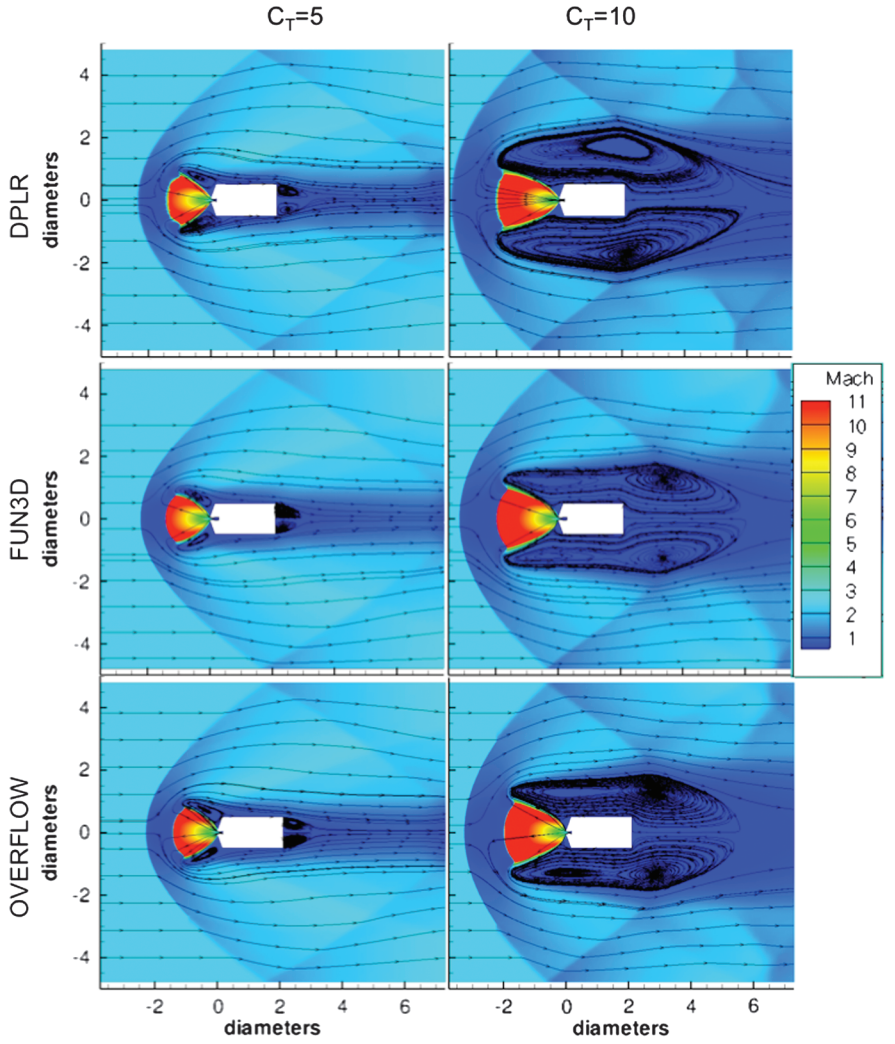

Fig. 12 Mach contours for single-nozzle configuration at $M_\infty = 2.4$ and $C_T = 5$ and 10.

general flowfield structure and both codes predicted relatively steady plumes. These codes also initialized the plume flow from the plenum of the nozzle. The plume predicted by DPLR was unsteady and initialized from the throat of the nozzle. The differences in nozzle flow initiation would affect the development of the boundary layer and subsequently the plume. The approach used to tackle these simulations was independently determined for each code; as a result, the nozzle flow initiation varies for each code from throat to plenum. FUN3D was run with local time stepping, whereas DPLR and OVERFLOW solutions were advanced using a global time stepping approach. Although DPLR and OVERFLOW both used global time stepping, the DPLR time step is an order of magnitude smaller than OVERFLOW, which may lead to the capture of unsteadiness of the nozzle plume.

Tunnel wall effects increase with higher thrust coefficients, lower Mach numbers, and with the larger model diameter (Fig. 4). Also, the 6-in.-diam model at high thrust coefficients and low Mach numbers

Table 2 Bow and termination shock standoff distances with percent difference for all nozzle configurations, thrust coefficients, and CFD codes

Case			Slice location	Bow shock			Max %	Termination shock			Max %
Nozzles	Mach	C_T		DPLR	FUN3D	OVERFLOW	Difference	DPLR	FUN3D	OVERFLOW	Difference
1	2.4	5	Center nozzle	2.33	2.23	2.31	4.48	1.40	1.39	1.41	1.44
		10		3.44	3.14	3.24	9.55	1.98	1.93	1.96	2.59
	4.6	5		2.13	2.15	2.16	1.41	1.34	1.46	1.45	8.96
		10		3.04	2.98	2.97	2.36	2.01	2.07	2.02	2.99
3	2.4	5	Peripheral nozzle	1.82	1.60	1.78	13.75	0.97	0.87	0.87	11.49
		10		2.82	2.51	2.70	12.35	1.42	1.27	1.35	11.81
	4.6	5		1.84	1.56	1.67	17.95	1.02	0.90	0.92	13.33
		10		2.80	2.24	2.34	25.00	1.50	1.33	1.29	16.28
4	2.4	5	Center nozzle	3.50	3.04	3.11	15.13	1.85	1.66	1.75	11.45
		10		8.21	3.96	7.75	107.32	3.88	2.38	3.90	63.87
	4.6	5		3.64	3.73	4.41	21.15	2.22	2.35	2.57	15.77
		10		5.72	5.78	6.28	9.79	3.48	3.68	3.87	11.21
4	2.4	5	Peripheral nozzle	3.31	2.24	2.9	47.77	1.17	0.78	1.28	64.10
		10		7.60	3.35	6.76	126.87	1.57	1.64	1.37	19.71
	4.6	5		3.16	2.82	3.03	12.06	1.15	1.07	1.10	7.48
		10		4.78	4.26	4.49	12.21	1.70	1.44	1.55	18.06

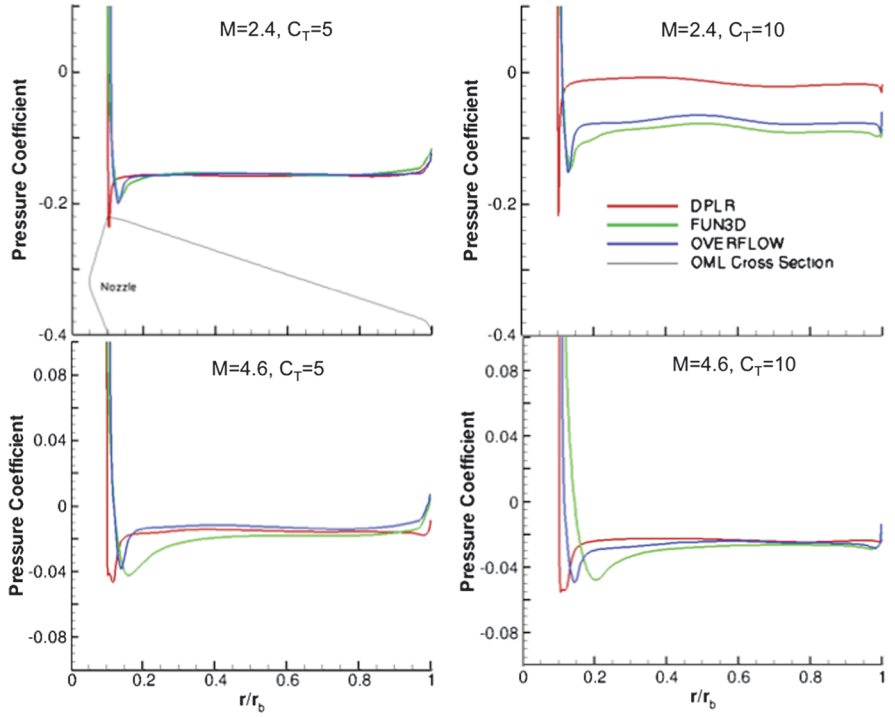

Fig. 13 Pressure coefficient slices for single-nozzle configuration at $M_\infty = 2.4$ and 4.6, $C_T = 5$ and 10.

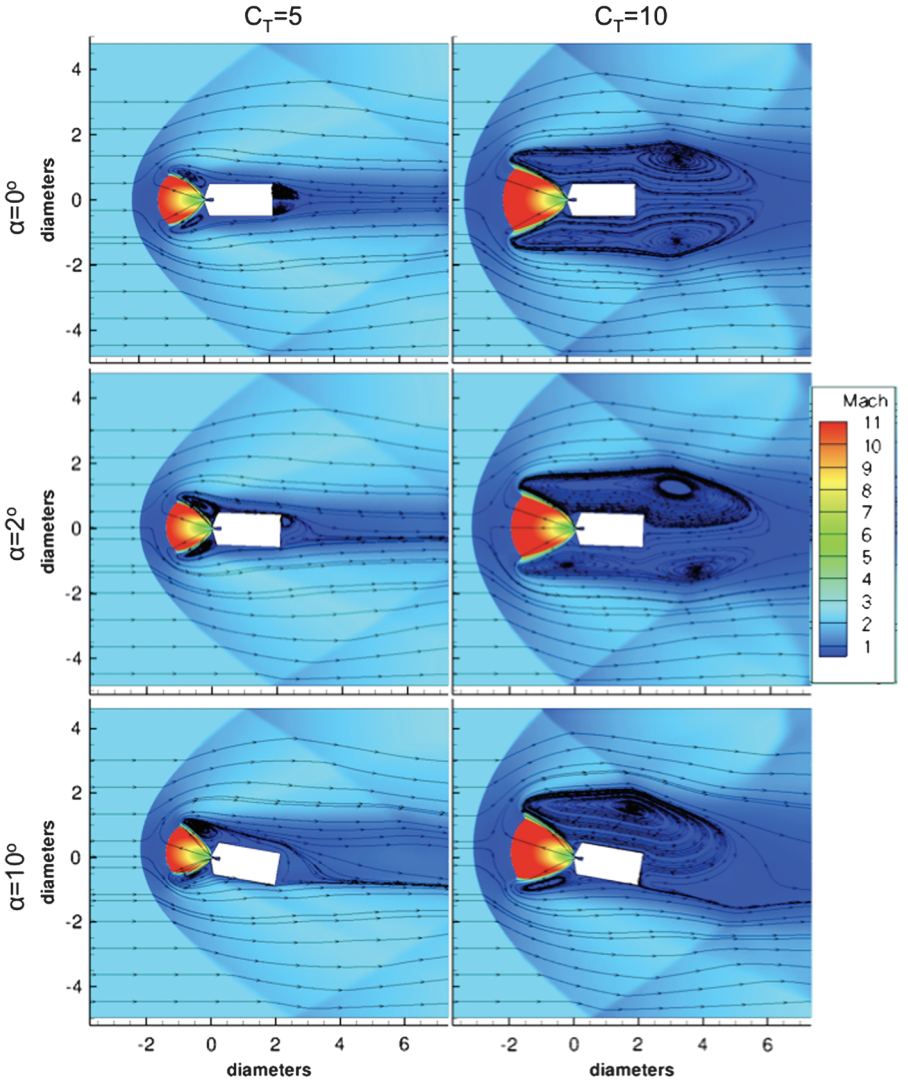

Fig. 14 Flowfield effects of angle of attack on single-nozzle configuration at $M_\infty = 2.4$ and $C_T = 5$ and 10. Only FUN3D is shown.

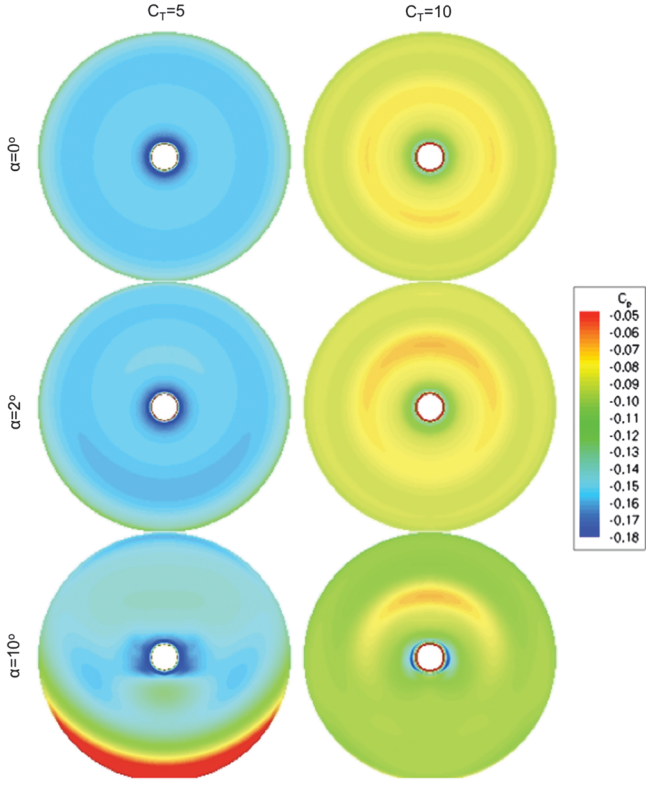

Fig. 15 Pressure coefficient contour effects from angle of attack on single-nozzle configuration at $M_\infty = 2.4$ and $C_T = 5$ and 10. Only FUN3D is shown.

became a candidate to cause tunnel blockage (Fig. 6), which could potentially damage the model instrumentation. The bow shock interacts with the tunnel wall creating a blockage effect, which induces the bow shock to move upstream. A 4 in. model was shown to be the better choice to minimize tunnel effects. However, this model was too small for packaging the internal instrumentation, and so a 5-in.-diam model was chosen as a compromise. The reduction in model diameter also resulted in the removal of the three-quarters radial peripheral nozzles due to internal packaging limitations.

The pretest CFD also aided in making corrective measures to avoid liquefaction. From CFD, temperatures within the plume were predicted to be as low as 10 K, raising concerns for the possibility of liquefaction of the air. To avoid the need to model two-phase flow, which would be out of the scope for this study, the nozzle area ratio was lowered from nine to four, and the nozzle gas in the plenum would be heated to help avoid liquefaction.

The internal flowpath in the plenum and fingers was simulated with FUN3D. The solution indicated flow separation downstream of the feed lines to the three-quarters radial peripheral nozzles (Fig. 7). In this simulation, the other nozzles are plugged and therefore contain no flow. To avoid separation, the internal corners within the flowpath for all nozzle configurations were smoothed and, as mentioned earlier, the three-quarters radial peripheral nozzles were removed.

IV. Pretest CFD Analysis

Once the model dimensions and nozzle configuration were chosen (Fig. 8), a matrix of pretest CFD cases was run to identify expected outcomes from the wind-tunnel experiment and also to assess code-to-code comparisons. The pretest CFD matrix is shown in Table 1. The test section was assumed symmetric and the tunnel walls were modeled inviscidly. The inviscid assumption is nonconservative

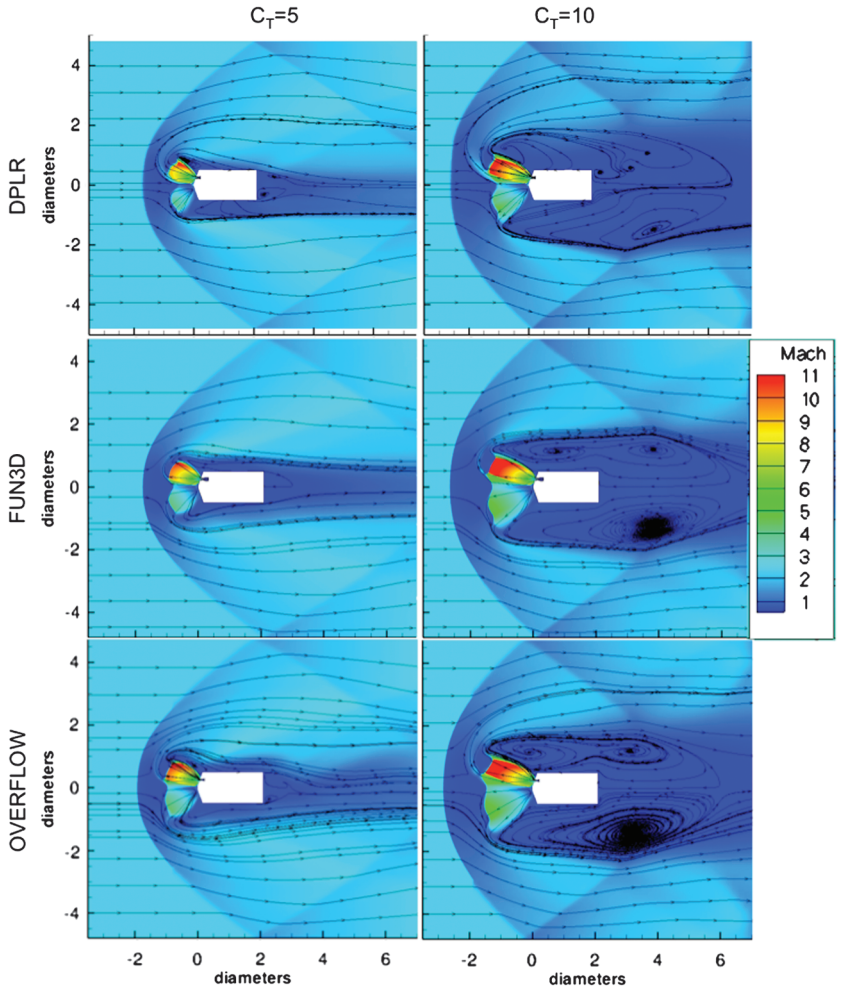

Fig. 16 Flowfield of three-nozzle configuration at $M_\infty = 2.4$ and $C_T = 5$ and 10 at zero angle of attack.

based on FUN3D calculations. A preliminary assessment of the tunnel boundary layer was performed with FUN3D by modeling the settling chamber, nozzle, and test section of the tunnel geometry with viscous walls at Mach 2.4. The FUN3D test section flowfield (Fig. 9) indicates that the desired freestream Mach of 2.4 has a thick boundary layer, which comprises nearly one-third of the tunnel test section.

A. Zero-Nozzle Configuration

As expected, good agreement between the codes is seen in the zero-nozzle configuration. This configuration is the well-understood supersonic blunt-body flow. Bow shock standoff distances are in agreement within the codes (Fig. 10). The surface pressure coefficients are in agreement on the flank region of the model, but differ the most at the nose (Fig. 11). For example, there is up to 4% disagreement on the nose for the case at $M_\infty = 4.6$ and $\alpha = 0$ deg, which are carbuncle effects at the stagnation point. As a reference, the theoretical normal shock pressure coefficient at the stagnation point is shown as the black symbols in the figure for $\alpha = 0$ deg.

B. Single Nozzle

For this configuration, a single nozzle is located at the center of the model, CFD solutions indicate that the largest amount of tunnel interference is shown at $M_\infty = 2.4$, $C_T = 10$, and $\alpha = 0$ deg (Fig. 12). At this test condition, Mach reflection off the wall occurs

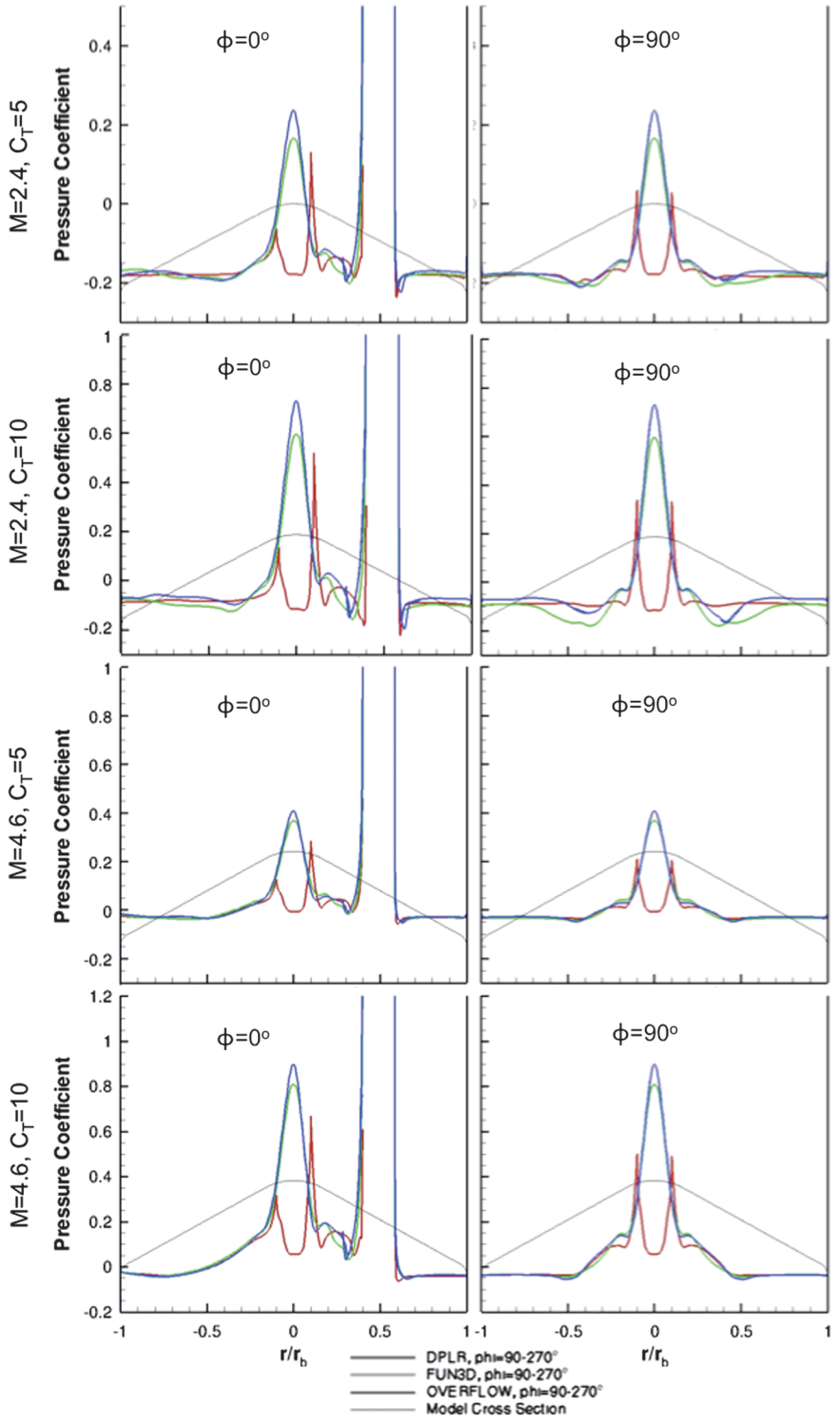

Fig. 17 Pressure coefficient slices for three-nozzle configuration model at zero angle of attack.

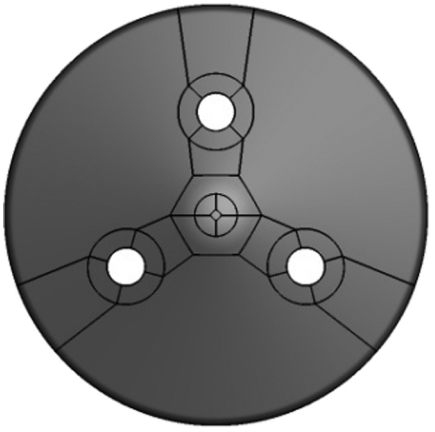

Fig. 18 DPLR grid topology for the three-nozzle configuration.

about one diameter length ahead of the model forebody. In contrast, at this same Mach number and $C_T = 5$, the Mach reflection occurs two diameter lengths downstream of the model forebody.

The three codes are in agreement with bow shock, termination shock, and interface locations (Table 2). The largest percent difference at $\alpha = 0$ deg in bow shock location is 9.5% for $M_\infty = 2.4$ and $C_T = 10$ and 9% in termination shock location for $M_\infty = 4.6$ and $C_T = 5$. The codes differ, however, in that DPLR predicts unsteadiness at the triple point, which is defined as the location where the shear layer from the plume, the termination shock, and the recirculation region meet. It could also be described as the corners of the plume. FUN3D consistently predicts steady flows. OVERFLOW predicts both steady and unsteady, varying case to case. The level of steadiness is reliant on the turbulence model, grid resolution, and time stepping. DPLR employs the vorticity-based SST model, whereas FUN3D and OVERFLOW use the strain-based SST model. All results presented here are instantaneous, regardless of the steadiness of the solution.

Pressure coefficients (Fig. 13) are in agreement for most of the single-nozzle cases. In the $M_\infty = 2.4$ and $C_T = 10$ case, the DPLR solution has a lower expansion ratio in the plume. The recirculation region in the DPLR solution is centered above the model, rather than behind as with FUN3D and OVERFLOW, and the reflection shocks are further upstream. This scenario creates a substantially higher pressure coefficient on the model surface for DPLR than for FUN3D and OVERFLOW, by as much as 92%. The difference between FUN3D and OVERFLOW is about 28%. The discrepancy in expansion ratio and pressure coefficient is isolated to this particular run and is not seen in any of the other cases.

The effects of angle of attack on the Mach reflections for $M_\infty = 2.4$ and $C_T = 5$ and 10 are shown in Fig. 14. Because results were typical, only FUN3D solutions are shown. The same trends are held for the other two codes. As the angle of attack is increased, the Mach reflection on the lower wall is pushed back by about one-half diameter length from 0 to 10 deg for both thrust coefficients. The Mach reflection on the upper wall, conversely, is moved one-half diameter length upstream. However, the change in Mach reflection location is greater between thrust coefficients than angles of attack. For $M_\infty = 2.4$, the Mach reflection is moved upstream two diameters when going from $C_T = 5$ to $C_T = 10$. The effects of angle of attack on the pressure coefficient are shown in Fig. 15. Again, only FUN3D solutions are shown. The differences in pressure coefficient between 0 and 2 deg are minimal; an asymmetry develops but the magnitude remains the same. At 10 deg, the pressure coefficient is increased significantly at $C_T = 5$ due to the oncoming flow having a direct path to the face of the model. The pressure coefficient at $C_T = 10$ is lowered due to greater separation on the face caused by the larger plume.

C. Three-Nozzle Configuration

This configuration consists of all three periphery nozzle jets on and the center nozzle plugged. The three-nozzle configuration analysis was only performed for zero angle of attack. Again the largest amount of tunnel interference is at $M_\infty = 2.4$, $C_T = 10$, and $\alpha = 0$ deg. Here, the Mach reflection off the tunnel wall occurs at the same axial location as predicted by all three codes (Fig. 16). The tunnel blockage for the three-nozzle configuration at this thrust coefficient is not as severe as the single-nozzle configuration.

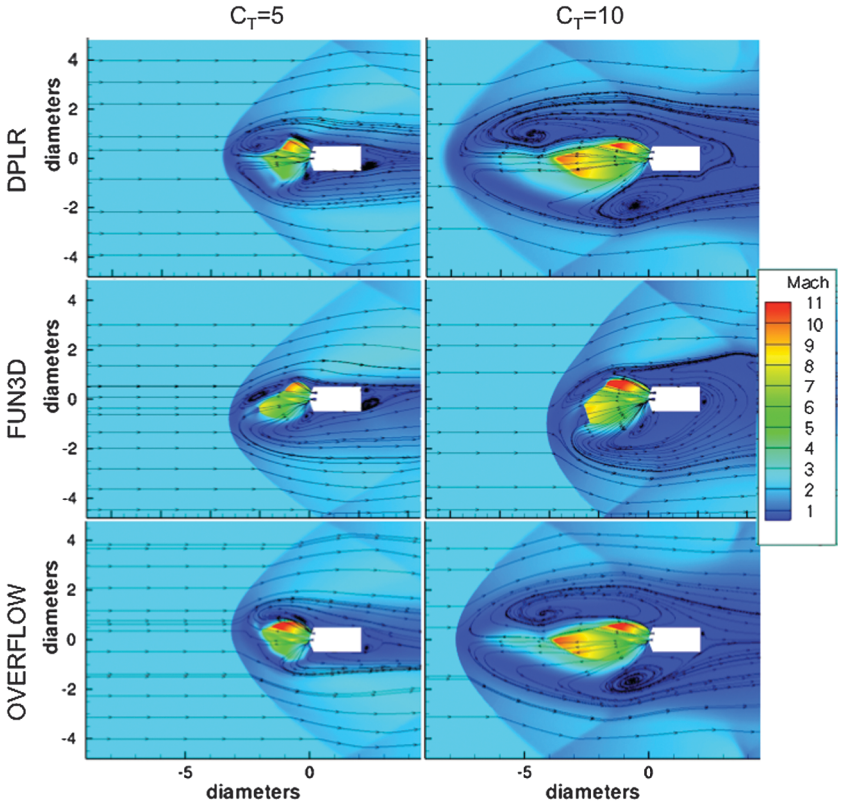

Fig. 19 Four-nozzle configuration flowfield at zero angle of attack at $M_\infty = 2.4$ and $C_T = 5$ and 10.

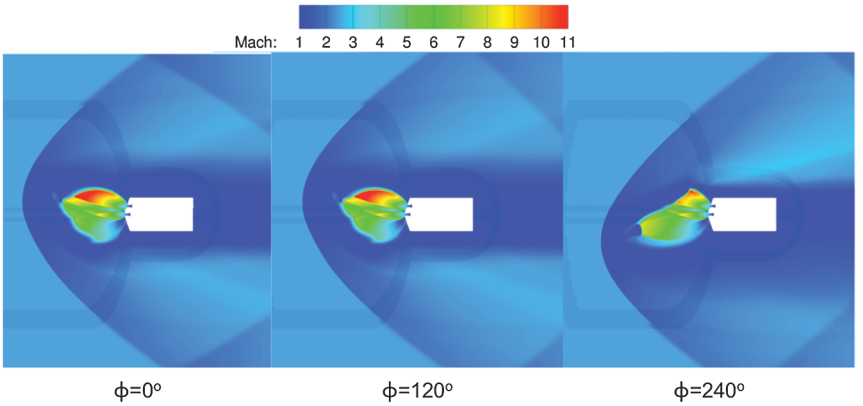

Fig. 20 Asymmetry in plume shown at slices through each peripheral nozzle for $M_\infty = 2.4$ and $C_T = 5$ in OVERFLOW.

The three codes predict similar locations of bow shock, interface, and termination shock (Table 2). The maximum percent difference in bow shock location is 25% for $M_\infty = 4.6$ and $C_T = 10$. DPLR and FUN3D predicted steady flow on this configuration. OVERFLOW is unsteady at all cases except for $M_\infty = 2.4$ and $C_T = 10$. Slices taken at $\phi = 0$ and 90 deg (Fig. 3) of the pressure coefficients, however, differ greatly at the nose, as seen in Fig. 17. The DPLR solution predicts significantly lower pressure coefficient on the nose. This discrepancy is a result of a boundary condition implementation error associated with the grid topology employed. The rise in pressure coefficient leading up to the nose is in accordance with FUN3D and OVERFLOW, and then there is a sharp decline at the boundaries of the nose due to the implementation error of the wall boundary condition. (Fig. 18). This is not seen in the single- or four-nozzle configurations because the boundary condition at this location is not modeled as a wall but rather a nozzle exit. This is not observed in the zero-nozzle case because the grid topology was entirely different from the nozzle cases. This is also not seen in follow-on three-nozzle configuration DPLR cases with different topologies [7,8,12,13]. The difference at the nose between FUN3D and OVERFLOW is about 30%. The outer flank region of the model is at a nearly constant pressure coefficient for all three codes. The spike in pressure coefficient at the nondimensional radial location of 0.5 is the location of the nozzle through slice $\phi = 0$ deg.

D. Four-Nozzle Configuration

The shock standoff distances and interface locations vary much more in the four-nozzle configuration cases than in the previous cases with fewer nozzles (Table 2), particularly for $M_\infty = 2.4$ (Fig. 19). In the $M_\infty = 2.4$ and $C_T = 5$ case, the bow shock location is similar between codes, but the plume structures are quite different. The OVERFLOW plume differs from DPLR and FUN3D. Upon further examination, an asymmetry in the OVERFLOW plume was found when comparing slices taken through each peripheral nozzle (Fig. 20). The OVERFLOW slice at $\phi = 240$ deg compares well with the shape of the DPLR and FUN3D solutions. The FUN3D solution was not able to determine asymmetry because it was run at a 180 deg revolution with a forced symmetry plane. DPLR was run at a 360 deg revolution and was symmetric when compared to slices through each peripheral nozzle. At $M_\infty = 2.4$ and $C_T = 10$, both DPLR and OVERFLOW predict

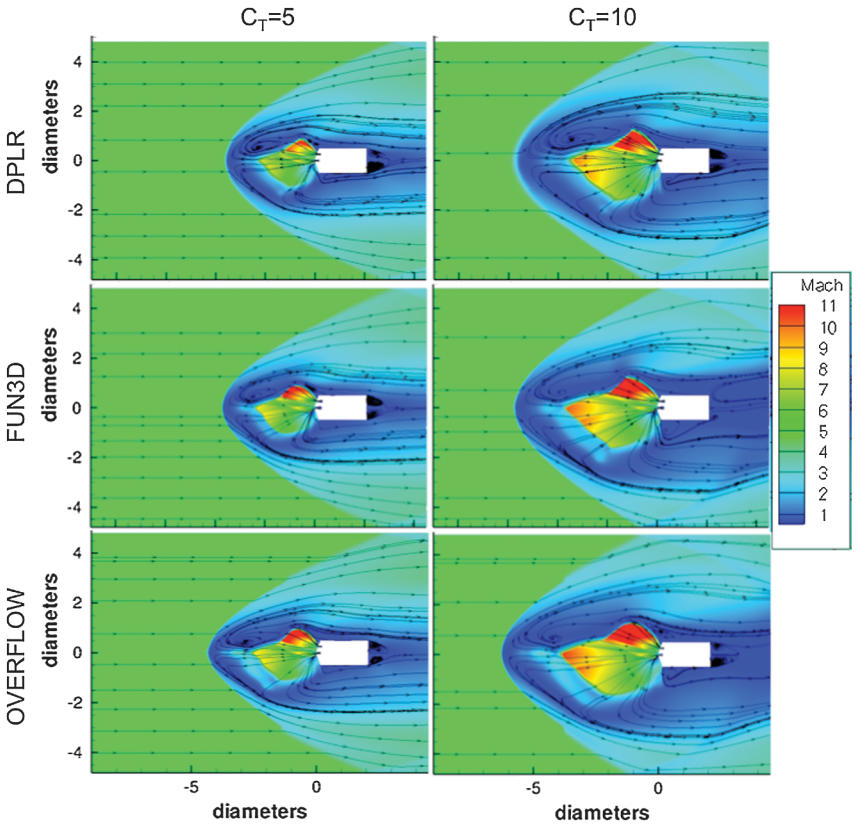

Fig. 21 Four-nozzle configuration flowfield at zero angle of attack at $M_\infty = 4.6$ and $C_T = 5$ and 10.

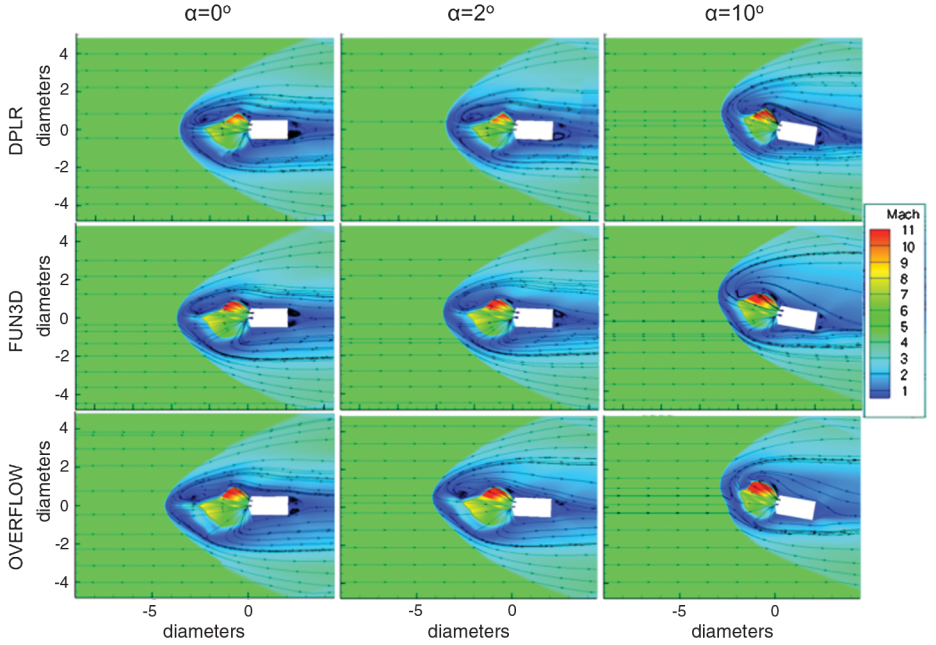

Fig. 22 Four-nozzle configuration flowfield at angle of attack at $M_\infty = 4.6$ and $C_T = 5$.

a long penetration plume mode where FUN3D contains a blunt termination shock. This results in a large difference in shock standoff distances and interface location. FUN3D predicts a bow shock location of about 4 diameters upstream, whereas DPLR and OVERFLOW are nearly twice that. The sequence of nozzle and freestream flow initialization was not consistent for the codes' running practices and could contribute to the jet mode seen. At $M_\infty = 4.6$ (Fig. 21), agreement between the codes becomes much better, particularly at $C_T = 10$. All three CFD codes predicted steady flow here. The presence of the center nozzle is attributed to the steadiness.

The effect of angle of attack on the flowfield of $M_\infty = 4.6$ and $C_T = 5$ is shown in Fig. 22. At angle of attack, the bow shock is no longer symmetric. A blunted edge forms on the bow shock, most evident in the $\alpha = 10$ deg case. As the angle of attack increases, the effective body diameter created by the plumes increases and pushes the bow shock out further. All CFD codes predict similar shock standoff distances and trend in the same manner.

V. Conclusions

The use of computational fluid dynamics can greatly advance the technology of supersonic retropropulsion. To build confidence in CFD for SRP flows, a series of wind-tunnel tests was designed to aid in the validation of these tools. The first in the series, at NASA Langley Unitary Plan Wind Tunnel, was designed with the help of CFD in determining model diameter, liquefaction avoidance measures, identifying potential tunnel blockage conditions, and nozzle layout design. The use of CFD in test and model design was also valuable in determining potential areas of modeling shortcomings and assessing the requirements necessary for computing these complex SRP flows.

Computational fluid dynamics aided the model design process by identifying the potential for tunnel blockage or unstart with a 6-in.-diam model at $M_\infty = 2.4$ and $C_T = 10$. This result led to the final chosen model diameter of 5 in. Computational fluid dynamics raised concerns about the issue of liquefaction within the plume and led to steps to minimize the likelihood of this occurring, such as heating the plenum and reducing the nozzle area ratio. The modeling of the internal manifolds suggested that separation would occur at the fingers of the nozzles. This resulted in the requirement to radius the corners at that location.

A pretest computational fluid dynamics case matrix was designed for the wind-tunnel Mach number range (2.4–4.6), desired angle-of-attack range (0, 2, and 10 deg), and thrust coefficient range (0, 5, and 10) with the final chosen 5 in. model diameter. The matrix was simulated with three computational fluid dynamics codes (DPLR, FUN3D, and OVERFLOW). Across all cases, the three codes predict similar flowfield structures, such as the location and characteristics of the jet termination shock, interface region, bow shock, and recirculation region. However, the codes most notably differ on the level of unsteadiness predicted. The turbulence models used in each code influenced the steadiness or lack of steadiness predicted. Although all three codes used the shear stress transport turbulence model, each had a slightly different version of the model. The DPLR turbulence model is vorticity based, whereas FUN3D and OVERFLOW turbulence models are strain based. The mode of jet, long penetration versus blunt termination, was also a difference between the codes for some of the cases. The initialization of flow in the nozzle with respect to the freestream flow could govern the jet mode.

In addition to the wind-tunnel experiment and model design support, the pretest study performed here also gave valuable information on CFD modeling practices and shortcomings for supersonic retropropulsion. A full three-dimensional domain is preferred to account for an asymmetry in the flow. Because of the unsteady nature of SRP flow, time accuracy, flow statistics, and averaging are necessary. Turbulence models can influence the shape of plumes and level of unsteadiness in the triple-point region. The sequence of nozzle and freestream flow initialization can dictate which jet mode, long penetration or blunt termination, is established.

Acknowledgments

The first author would like to thank Michael Barnhardt and Todd White for support on DPLR best practices and Andrew J. Hyatt for overset gridding assistance. The second author would like to thank Pieter Buning, Phil Stuart, Tom Booth, and Darby Vicker for valuable guidance on gridding and solver best practices. The third author would also like to thank William T. Jones of NASA Langley Research Center for enabling very rapid unstructured grid generation thanks to his GridEx/batchEx software. Time from geometry to grid was typically less than a day and even then the lion's share was due to serial volume grid generation and not user interaction.

References

[1] Braun, R. D., and Manning, R. M., "Mars Exploration Entry, Descent, and Landing Challenges," *Journal of Spacecraft and Rockets*, Vol. 44, No. 2, 2007, pp. 310–323. doi:10.2514/1.25116

[2] Steinfeldt, B. A., Theisinger, J. E., Korzun, A. M., Clark, I. G., Grant, M. J., and Braun, R. T., "High Mass Mars Entry, Descent, and Landing Architecture Assessment," AIAA Paper 2009-6684, Sept. 2009.
[3] Zang, T. A., Dwyer-Dianciolo, A. M., Kinney, D. J., Howard, A. R., Chen, G. T., Ivanov, M. C., Sostaric, R. R., and Westhelle, C. H., "Overview of the NASA Entry, Descent and Landing Systems Analysis Study," AIAA Paper 2010-8649, Aug. 2010.
[4] Edquist, K. T., Korzun, A. M., Dyakonov, A. A., Shidner, J. D., Studak, J. W., Tigges, M. A., Kipp, D. M., Prakash, R., Zarchi, K. A., and Dupzyk, I. C., "Development of Supersonic Retropropulsion for Future Mars Entry Descent and Landing Systems," *Journal of Spacecraft and Rockets* (to be published).
[5] Korzun, A. M., and Braun, R. D., "Performance Characterization of Supersonic Retropropulsion Technology for High-Mass Mars Entry Systems," *Journal of Spacecraft and Rockets*, Vol. 47, No. 5, 2010, pp. 836–848. doi:10.2514/1.49803
[6] Korzun, A. M., Braun, R. D., and Cruz, J. R., "Survey of Supersonic Retropropulsion Technology for Mars Entry, Descent, and Landing," *Journal of Spacecraft and Rockets*, Vol. 46, No. 5, 2009, pp. 929–937. doi:10.2514/1.41161
[7] Schauerhamer, D. G., Zarchi, K. A., Kleb, W. L., Carlson, J. R., and Edquist, K. T., "Supersonic Retropropulsion CFD Validation with Langley $4' \times 4'$ Unitary Plan Wind Tunnel Test Data," *Journal of Spacecraft and Rockets* (to be published).
[8] Kleb, W. L., Carlson, J. R., Buning, P. G., Berry, S. A., Rhode, M. N., Edquist, K. T., Schauerhamer, D. G., Zarchi, K. A., and Sozer, E., "Toward Supersonic Retropropulsion CFD Validation," *Journal of Spacecraft and Rockets* (to be published).
[9] Schauerhamer, D. G., Zarchi, K. A., Kleb, W. L., and Edquist, K. T., "Supersonic Retropropulsion CFD Validation with Ames $9' \times 7'$ Unitary Plan Wind Tunnel Test Data," *Journal of Spacecraft and Rockets*, 2014. doi:10.2514/1.A32694
[10] Jarvinen, P. O., and Adams, R. H., "Aerodynamic Characteristics of Large Angled Cones with Retrorockets," NASA NAS7-576, Feb. 1970.
[11] Trumble, K. A., Schauerhamer, D. G., Kleb, W. L., Carlson, J. R., Buning, P. G., Edquist, K. T., and Barnhardt, M. D., "Initial Assessment of Navier–Stokes Codes Applied to Supersonic Retro-Propulsion," AIAA Paper 2010-5047, June 2010.
[12] Zarchi, K. A., Schauerhamer, D. G., Kleb, W. L., Carlson, J.-R., and Edquist, K. T., "Computational Fluid Dynamics Validation and Post-Test Analysis of Supersonic Retropropulsion in the Ames 9×7 Unitary Tunnel," AIAA Paper 2012-2705, June 2012.
[13] Schauerhamer, D. G., Zarchi, K. A., Kleb, W. L., and Edquist, K. T., "Supersonic Retropropulsion CFD Validation with Ames 9×7 Unitary Plan Wind Tunnel Test Data," *Journal of Spacecraft and Rockets* (to be published).
[14] Wright, M. W., White, T., and Mangini, N., "Data Parallel Line Relaxation (DPLR) Code User Manual Acadia–Version 4.01.1," NASA TM-2009-215388, Oct. 2009.
[15] Anderson, W. K., and Bonhaus, D. L., "Implicit Upwind Algorithm for Computing Turbulent Flows on Unstructured Grids," *Journal of Computational Physics*, Vol. 128, No. 2, 1996, pp. 391–408. doi:10.1006/jcph.1996.0219
[16] Anderson, W. K., Rausch, R. D., and Bonhaus, D. L., "Implicit/Multigrid Algorithm for Incompressible Turbulent Flows on Unstructured Grids," *Journal of Computational Physics*, Vol. 128, No. 2, 1996, pp. 391–408. doi:10.1006/jcph.1996.0219
[17] Buning, P. G., Jespersen, D. C., Pulliam, T. H., Klopfer, G. H., Chan, W. M., Slotnick, J. P., Krist, S. E., and Renze, K. J., *Overflow User's Manual*, NASA Langley Research Center, Hampton, VA, 2002.
[18] Berry, S. A., Rhode, M. N., Edquist, K. T., Player, C., Laws, C. T., Kleb, W. L., Spells, C., Mccrea, A. C., Trumble, K. A., Schauerhamer, D. G., and Oberkampf, W. L., "Design and Analysis of a Supersonic Retropropulsion Validation Experiment in the NASA Langley Unitary Plan Wind Tunnel," *Journal of Spacecraft and Rockets* (to be published).
[19] MacCormack, R. W., and Candler, G. V., "Solution of the Navier–Stokes Equations Using Gauss-Seidel Line Relaxation," *Computers and Fluids*, Vol. 17, No. 1, 1989, pp. 135–150. doi:10.1016/0045-7930(89)90012-1
[20] Yee, H. C., "Class of High-Resolution Explicit and Implicit Shock Capturing Methods," NASA TM-101088, Feb. 1989.
[21] Menter, F. R., "Two-Equation Eddy-Viscosity Turbulence Models for Engineering Applications," *AIAA Journal*, Vol. 32, No. 8, 1994, pp. 1598–1605. doi:10.2514/3.12149
[22] Edwards, J. R., "Low-Diffusion Flux-Splitting Scheme for Navier–Stokes Calculations," *Computers and Fluids Journal*, Vol. 26, No. 6, 1997, pp. 653–659. doi:10.1016/S0045-7930(97)00014-5
[23] Benek, J. A., Buning, P. G., and Steger, J. L., "3-D Chimera Grid Embedding Technique," AIAA Paper 1985-1523, 1985.
[24] Chan, W. M., Gomez, R. J. III, Rogers, S. E., and Buning, P. G., "Best Practices in Overset Grid Generation," AIAA Paper 2002-3191, June 2002.
[25] Jespersen, D. C., Pulliam, T. H., and Buning, P. G., "Recent Enhancements to Overflow (Navier–Stokes Code)," AIAA Paper 1997-0644, Jan. 1997.
[26] Tramel, R., Nichols, R., and Buning, P.G., "Addition of Improved Shock-Capturing Schemes to Overflow 2.1," *19th AIAA Computational Fluid Dynamics*, AIAA Paper 2009-3988, June 2009.
[27] Pulliam, T. H., and Chaussee, D. S., "Diagonalized Form of an Implicit Approximate Factorization Algorithm," *Journal of Computational Physics*, Vol. 39, No. 2, 1981, pp. 347–363 doi:10.1016/0021-9991(81)90156-X
[28] Nichols, R., Tramel, R., and Buning, P., "Solver and Turbulence Model Upgrades to Overflow 2 for Unsteady and High-Speed Applications," AIAA Paper 2006-2824, June 2006.
[29] Pandya, S. A., Venkateswaran, S., and Pulliam, T. H., "Implementation of Preconditioned Dual-Time Procedures in Overflow," AIAA Paper 2003-0072, Jan. 2003.
[30] Baldwin, B. S., and Barth, T. J., "One-Equation Turbulence Transport Model for High Reynolds Number Wall-Bounded Flows," AIAA Paper 1991-0610, Jan. 1991.
[31] Spalart, P. R., and Allmaras, S. R., "One-Equation Turbulence Model for Aerodynamic Flows," AIAA Paper 1992-0439, Jan. 1992.
[32] Meakin, R. L., "Object X-Rays for Cutting Holes in Composite Overset Structured Grids," AIAA Paper 2001-2537, June 2001.
[33] Jespersen, D. C., "Parallelism and Overflow," NASA Advanced Supercomputing (NAS) TR-NAS-98-013, Oct. 1998.
[34] Meakin, R. L., "Automatic Off-Body Grid Generation for Domains of Arbitrary Size," AIAA Paper 2001-2536, June 2001.
[35] Meakin, R. L., "Efficient Means of Adaptive Refinement within Systems of Overset Grids," AIAA Paper 1995-1722, June 1995.
[36] Murman, S., Chan, W. M., Aftosmis, M. J., and Meakin, R. L., "Interface for Specifying Rigid-Body Motions for CFD Applications," AIAA Paper 2003-1237, Jan. 2003.
[37] Meakin, R. L., "Multiple-Body Proximate-Flight Simulation Methods," AIAA Paper 2005-4621, June 2005.
[38] Tramel, R., Nichols, R., and Buning, P. G., "Addition of Improved Shock-Capturing Schemes to OVERFLOW 2.1," AIAA Paper 2009-3988, June 2009.
[39] van Albada, G. D., van Leer, B., and Roberts, W. W., "Comparative Study of Computational Methods in Cosmic Gas Dynamics," *Astronomy and Astrophysics*, Vol. 108, No. 1, 1982, pp. 76–84.

C.-L. Chang
Associate Editor